1 **Recreating the Biological Steps of Viral Infection on a Bioelectronic**

2 **Platform to Profile Viral Variants of Concern**

3

4 *Zhongmou Chao,[1†] Ekaterina Selivanovitch,[1†] Konstantinos Kallitsis,[2] Zixuan Lu,[2] Ambika*

5 *Pachaury,[1] Róisín Owens,[2] Susan Daniel[1]**

6

7 [1] Robert Frederick Smith School of Chemical and Biomolecular Engineering, Cornell University,

8 124 Olin Hall, Ithaca, NY 14853, USA

9 [2] Department of Chemical Engineering and Biotechnology, University of Cambridge, Philippa

10 Fawcett Dr., Cambridge CB3 0AS, UK

11

12 † These authors contributed equally to this work.

13 * Corresponding author. Email: sd386@cornell.edu

14

15

16 **Abstract**

17 Viral mutation rates frequently outpace the development of technologies used to detect and

18 identify harmful variants; for SARS Coronavirus-2 (SARS-CoV-2), these are called variants of

19 concern (VOC). Given the continual emergence of VOC, there is a critical need to develop

20 platforms that can identify the presence of a virus and readily identify its propensity for

21 infection. We present an electronic biomembrane sensing platform that recreates the multifaceted

22 and sequential biological cues that give rise to distinct SARS-CoV-2 virus host cell entry

23   pathways and reports the progression of entry steps of these pathways as electrical signals.

24   Within these electrical signals, two necessary entry processes mediated by the viral Spike

25   protein, virus binding and membrane fusion, can be distinguished. Remarkably, we find that

26   closely related VOC exhibit distinct fusion signatures that correlate with trends reported in cell-

27   based infectivity assays, allowing us to report quantitative differences in fusion characteristics

28   among them that inform their infectivity potentials. This cell-free biomimetic infection platform

29   also has a virus-free option that equally reports infectivity potential of the Spike proteins. We

30   used SARS-CoV-2 as our prototype, but we anticipate that this platform will extend to other

31   enveloped viruses and cell lines to quantifiably explore virus/host interactions. This advance

32   should aid in faster determination of entry characteristics and fusogenicities of future VOC,

33   necessary for rapid response.

34

Introduction

36   RNA viruses tend to have high mutation rates than their DNA counterparts[1-3], hence developing

37   vaccines and antivirals that remain protective against disease-causing viral variants remains

38   challenging with the fast pace of emerging variants of concern (VOC). When outbreaks of new

39   viruses occur, quickly establishing the mechanisms of viral entry and transmission are critical for

40   the rapid development of vaccines and therapeutics to combat RNA viruses and assessing

41   emerging VOC and determining their potential for human harm. However, doing this is no easy

42   feat; the mechanisms of viral infection are complex, involving numerous, multi-step biological

43   processes, which often vary across cell types and microenvironments, hence necessitating a

44   protracted incubation period for comprehensive data acquisition by live cell-based assays[4-6]. The

45   entry pathway chosen by SARS-CoV-2, for example, is highly dependent on the interactions at

46   the host cell membrane-virion interface, as well as the local protease, pH, and ionic conditions[7].

47   Because viral entry represents the first contact viruses have with host cells, the proteins and

48   mechanisms that comprise these events have been targeted therapeutically and diagnostically to

49   block or detect viral infection.

50   The last few years have witnessed a surge of advancements aimed towards the rapid,

51   sensitive, and accurate detection of viruses and their emerging variants. While Reverse

52   Transcription Polymerase Chain Reaction (RT-PCR)[8] remains the gold standard for detection,

53   other classical methods include antibody detection[9], which relies on detecting antigen specific

54   antibodies in serum, and antigen detection[10], which uses designer antibodies to bind to and detect

55   antigens. While these methods have been instrumental throughout the COVID-19 pandemic, they

56   provide a binary response indicating either a detectable presence or absence of an antigen but

57   offer few insights into their infectivity potential and are not appropriate for screening VOC.

58   Furthermore, studies have shown that as variants emerge, the ability of designed primers and

59   antibodies to maintain their sensitivity diminishes, requiring the detection materials to be

60   reformulated[11]. CRISPR-Cas- and isothermal amplification-based detection technologies have

61   also been developed[12,13]. Techniques that fall into both categories detect nucleic acid (RNA or

62   DNA) sequences and, while offering high sensitivity and selectivity, do not offer insights into a

63   virus' structural integrity. Biosensors, on the other hand, have been shown to differentiate

64   between a virus protein and a whole virus particle. They have been successfully used as detection

65   platforms for coronaviruses by exploiting the specificity of antigens for their respective

66   receptors[14-17]. However, to comprehensively understand the unique properties of emerging

67   mutants and their potential for infection beyond mere binding interactions, a functional

68   assessment of infectivity potential is imperative.

69   For enveloped viruses, which contain a lipid membrane that wraps or "envelopes" the

70   genome-filled capsid, infection of the host cell is initiated when virions first bind to a host cell

71   receptor, followed by the triggered fusion of the viral membrane with that of the host. These

72   critical entry steps (binding and fusion) allow for the viral genome to be delivered to the host's

73   cytosol. Chemically-responsive glycoproteins that protrude from the viral envelope mediate

74   these entry processes. Their interactions with the cell plasma membrane receptors and other

75   chemical cues create a fusion-promoting microenvironment. The cues that lead to viral entry

76   typically involve some sequence of exposure to receptors, specific proteases, low pH, and ions.

77   Depending on the host cell type, the identity of the triggers and the sequence of their presentation

78   can vary. Additionally, the glycoprotein's properties (*i.e.,* mutations that alter the glycoprotein in

79   some way) also influence how they respond to these cues. Thus, it is a complicated convolution

80   of glycoprotein sequence and host cell environment that control the entry of these viruses and

81   ultimately create conditions for a productive infection of the host. Coronaviruses (including

82   SARS-CoV, MERS and SARS-CoV-2), are a family of enveloped viruses and the variety of

83   conditions that influence their biological entry pathways represent a major hurdle in probing

84   viral infection mechanisms *in vivo*, as many methods lack the necessary control of the

85   microenvironmental conditions and clear signals of a successful entry process. To gain the upper

86   hand in mitigating future virus outbreaks and staying ahead of emerging VOC, it is crucial to

87   develop platforms that are capable of both mimicking infection conditions and reporting

88   infection progress via quantifiably readouts.

89   Here, we demonstrate the power of a new technique that can detect viral entry processes,

90   but importantly, provide quantitative readouts that distinguish entry characteristics of closely-

91   related viral strains. Starting with SARS-CoV-2 Wuhan-Hu-1 (WH1) as a model target, we

92   present the design of an *in vitro*, cell-free entry platform (with a virus-free option as well) based

93   on supported lipid bilayers (SLBs) that faithfully replicates the conditions that promote entry but

94   in a convenient, controllable, and tailorable format with a much faster response time than live

95   cell assays. This cell-free platform senses entry functions electrically and is thus label-free. Next,

96   we probe the entry characteristics of two SARS-CoV-2 Omicron subvariants, Omicron BA.1 and

97   Omicron BA.4, and show that our platform identifies the known differences in fusion activity

98   between these strains as well as repeats the known trends in their cell infectivity. This

99   demonstration of using bioelectronics for detecting and characterizing virus-host entry processes

100   is a critical precursor of the events that lead to host infection. Our device, mimicking the earliest

101   events in "*infection-on-a-chip*", opens possibilities for examining entry conditions that can be

102   leveraged for both basic science studies, screening assays for antiviral therapies, and fast

103   assessment of entry characteristics that can inform next steps in combatting VOC as they

104   emerge.

105

106   Results

107   A description of the biological pathways of SARS-CoV-2 entry that are recreated in this
108   platform

109   The exterior glycoprotein of SARS-CoV-2 is called Spike[18]. After the initial binding event

110   between Spike and the host cell receptor (membrane-bound angiotensin-converting enzyme 2

111   (ACE2), viral entry continues via one of two entry pathways depending on its spatiotemporal

112   exposure to microenvironmental cues[19]. Fig. 1 briefly summarizes the two identified pathways

113   for SARS-CoV-2 infection and the critical extra- and intracellular conditions that distinguish

114   them, specifically focusing on the initial steps of binding to, and fusion with, the host cell's

115   membrane. Which one of two entry pathways is triggered is cell type specific and based on the

116   availability of proteases for S2 cleavage. The first pathway, referred to here as the early entry

117   pathway, is initiated when the transmembrane serine protease 2 (TMPRSS2) is present in the

118   plasma membrane of the host cell[20]. Upon the binding of Spike protein to ACE2, the Spike is

119   cleaved by TMPRSS2 to initiate virus-host membrane fusion presumably at or near the cell

120   surface and the viral genome is delivered to the cytosol. The second pathway, referred to here as

121   the late entry pathway, proceeds when the membrane-bound protease is not present in the plasma

122   membrane of the host cell[21]. In this scenario, Spike protein binds to ACE2 and the virion is

123   endocytosed, where it is subsequently cleaved by the endosomal cysteine protease-cathepsin L

124   (CatL) inside the low pH microenvironment of the endosome. These cues trigger the fusion of

125   the viral envelope with the endosomal membrane and release the genome into the cytosol.

126

127   **Design Parameters for an *Infection-on-Chip* Device**

128   Taking inspiration from biological mechanisms, we set out to design a platform that can

129   faithfully reproduce the microenvironments needed to selectively trigger either of the two entry

130   pathways, and thus initiate the primary steps in a viral infection. There are four essential

131   components in the construction of this *infection-on-chip* platform: 1) the presentation of viral and

132   host cell membrane components, 2) spatiotemporal control over environmental cues required for

133   triggering fusion, 3) a biocompatible scaffold accommodating membrane components for

134   successful infection and 4) quantifiable readouts reflective of different infection stages.

135   To test the *infection-on-chip* platform for its ability to recapitulate specific cell membrane

136   environments that induce CoV entry events, we used Spike$_{WH1}$-incorporated viral

137   pseudoparticles (VPP$_{WH1}$), produced using previously established methods[22]. Confirmation of

138   Spike protein incorporation is included in Supplementary Fig. 1. To capture the host cell features

139   required for entry, but in a cell-free format, we selected SLB to serve as host cell membrane

140   mimics. These SLBs were composed from native cell membrane components (collected as

141   plasma membrane blebs, or cell blebs) and "fusogenic" lipid vesicles, which self-assemble into a

142   planar, single-bilayer lipid membrane blended with native cell membrane components, *i.e.,*

143   ACE2 receptors and TMPRSS2 proteases. The fusogenic vesicles used in this work are

144   reconstituted from purified 1-oleoyl-2-palmitoyl-*sn*-glycero-3-phosphocholine (POPC) lipids,

145   which is the principal lipid component of mammalian and viral membranes. As shown in Fig. 1,

146   this versatile, easy-to-assemble biomimetic membrane allowed spatiotemporal control over

147   environmental cues to recapitulate both early and late entry pathways: when cell blebs containing

148   ACE2 and TMPRSS2 (confirmed as shown in Supplementary Fig. 1) are incorporated into the

149   SLB, colocalizing receptors and membrane proteases, the early entry pathway can be accessed.

150   When SLBs are formed with only ACE2 containing blebs (confirmed as shown in

151   Supplementary Fig. 1), only fusion via late entry pathway can be activated when CatL is added

152   under acidic conditions.

153   SLBs can be readily self-assembled on various functional supports, including

154   biocompatible conductive polymers, which prompted our design of a label-free *SLB-on-electrode*

155   structure to directly translate the interactions occurring at the biomimetic membrane into an

156   electrical readout. Our group has previously demonstrated that SLBs can form on PEDOT:PSS

157   (poly(3,4-ethylenedioxythiophene) polystyrene sulfonate) supports[23,24], a conductive, transparent

158   polymer mixture widely used in biosensing applications[25,26]. We have also demonstrated that

159   SLBs prepared on these polymer supports maintain two-dimensional fluidity of the constituents

160   (both lipids and membrane proteins) and that the buffer-swollen polymer serves as a cushion that

161   supports this characteristic of cell membranes in the resultant SLB[24].

162   Presented in the following sections, we fulfill all design parameters necessary for

163   capturing SARS-CoV-2 *infection-on-chip* in a cell-free and label-free manner by building a

164   biomembrane bioelectronic platform. We demonstrate that the label-free electrical readouts of

165   this platform can provide a quantitative approach that could be used for investigating emerging

166   variants, identifying potential variants of concern, and potentially thwarting the progression of

167   outbreaks. For example, the platform could be used as a tool to discover means to disrupt or

168   arrest viral entry processes in anti-viral drug development, or in efforts to classify and

169   differentiate properties of emerging variants as strains evolve, which can assist in predicting host

170   tropism susceptibilities, or inform next generation formulations of vaccines.

171

Characterization of the *Infection-on-Chip* Device

173   The sizes of VPP$_{WH1}$, cell blebs, and synthetic POPC vesicles were measured using Dynamic

174   Light Scattering (DLS) and Nano Particle Analysis (NTA), and are reported to be approximately

175   100- 200 nm, 150- 450 nm, and 100 nm, respectively (Supplementary Fig. 2 and Supplementary

176   Fig. 3). The particles count, provided by NTA analysis, allowed us to control the relative

177   concentrations of the VPP$_{WH1}$ and blebs used to assemble the SLBs.

178   The method of forming SLBs from cell blebs and POPC vesicles on a PEDOT:PSS

179   support is described in **Methods**. To assess their formation, we used fluorescence recovery after

180   photobleaching (FRAP) measurements to confirm the formation of a mobile bilayer on

181   PEDOT:PSS-coated glass coverslips — a critical prerequisite for the fusion events described

182   later in this paper. For this optical characterization, SLBs formed on PEDOT:PSS surface were

183   labeled with a lipophilic dye, R18, and in the case of a mobile bilayer, the R18 dye should

184   diffuse freely throughout the SLB plane. Fig. 2a shows typical FRAP data showing the full

185   recovery of a photobleached spot on a SLB assembled using Vero E6 cell blebs and POPC

186   vesicles. Vero E6 cells were chosen due to their endogenous expression of ACE2; therefore, the

187   SLBs formed using blebs derived from this cell line incorporated the ACE2 receptor[27,28]. The

188   other SLBs assembled for our study were derived from recombinant Vero E6 cells containing the

189   TMPRSS2 receptor, and HEK 293 cells used to assemble Spike-incorporating SLBs. We chose a

190   TMPRSS2-modified Vero E6 cell line for the early entry pathway to remain consistent across as

191   many parameters as possible for comparison with the late entry pathway using Vero E6 cells[29,30].

192   The FRAP images for these SLBs on PEDOT:PSS can be found in Supplementary Fig. 4 and

193   Supplementary Fig. 5. Upon photobleaching, the fluorescent intensity as a function of time in the

194   photobleached spot was collected and fit with a Bessel function expression (see **Methods**) to

195   later calculate the diffusion coefficient, D. All SLBs show comparable diffusion coefficients:

196   ranging from 0.16-0.2 $\mu m^2/s$ and 0.92-0.99 mobile fractions (Supplementary Fig. 6).

197   To confirm the ACE2 receptors were incorporated into the SLBs, additional

198   characterization of our SLBs was conducted using total internal reflection fluorescence (TIRF)

199   microscopy. TIRF is an optical imaging technique especially suited to study the interactions

200   occurring near the SLB-bulk interface, as its induced evanescent wave illuminates a limited (~

201   100 nm) vertical region from this interface, effectively eliminating fluorescence from the bulk

202   emanating from unbound virus particles. Although our ultimate goal here is to validate a label-

203   free sensing platform for virus, the visualization of binding events between ACE2 and VPP$_{WH1}$

204   was necessary to verify that native cell receptors from blebs were incorporated into the SLB

205   assembled on PEDOT:PSS. VPP$_{WH1}$ were labeled with R18 fluorophores that partition into the

206   VPP membrane envelope; the SLB was not labeled in this experiment. We used TIFR

207   microscopy to measure specific interaction between ACE2 receptors in the SLBs and

208   fluorescently labeled VPP_{WH1}. As shown in Fig. 2b, a representative TIRF field of view (FOV)

209   provided evidence that the R18-labeled VPP_{WH1} are specifically bound to the ACE2 assembled

210   SLB, while particles devoid of Spike proteins ($VPP_{\Delta env}$) do not exhibit any detectable signals, as

211   a control case.

212   PEDOT:PSS is not only conductive, it is also a volumetric capacitor — making it an ideal

213   electrode material for electrochemical impedance spectroscopy (EIS) measurements as it

214   significantly reduces system impedance[31]. Lower system impedance enables the measurement of

215   small changes in SLB electrical properties that can be correlated with viral entry processes, as we

216   describe later. EIS is a non-invasive electrical sensing technique with a proven track record for

217   accurately quantifying bio-recognition events occurring at biointerfaces[32-34]. When a SLB is self-

218   assembled on PEDOT:PSS electrodes, the ionic flux reaching the electrode surface is reduced

219   due to SLB shielding, thereby decreasing the ionic current. This outcome is ultimately measured

220   by an increase in circuit impedance when compared to the electrode baseline signal (a circuit

221   without SLB coating). The PEDOT:PSS electrodes used in this work were defined on a gold

222   contact pad using optical lithography (see **Methods**). As shown in Fig. 2c, when no SLB was

223   formed on the PEDOT:PSS electrode, the circuital response to alternating voltage with changing

224   frequency is plotted in black, generating a "hockey stick" shape bare electrode baseline signal

225   (PEDOT:PSS only), indicating a typical resistor-capacitor in series structure. Upon the self-

226   assembly of a SLB on the electrode (+Vero SLB), the circuital response shifted from black

227   "hockey stick" to red "chair shape", confirming the addition of a resistor-capacitor in parallel

228   structure — an established electrical trait of lipid bilayers[35,36]. The membrane resistance (R_m)

229   and capacitance (C_m) of the SLB can then be extracted by fitting the signal into an equivalent

230   electrical circuit, as depicted, and then normalized by the area of the electrode.

231

232   **Recreating the SARS-CoV-2 Entry Pathways using *Infection-on-Chip***

233   Now that we have formed a mobile SLB with confirmed native membrane components using

234   FRAP, demonstrated that the initial steps in SARS-CoV-2 infection process (*i.e.,* binding) using

235   TIRF, and verified that SLB-formation results in a measurable signal using EIS, we continued to

236   investigate if fusion can be initiated and detected on our chip when environmental cues are

237   integrated spatiotemporally.

238   We first focused on the early entry pathway where we mimicked the respective fusion

239   triggering environment by forming a SLB from cell blebs containing ACE2 and TMPRSS2 on

240   the PEDOT:PSS surface. We then introduced the VPP$_{WH1}$ to monitor binding and fusion as

241   depicted in the schematic shown in Fig. 3a. Electrical readouts were conducted on PEDOT:PSS

242   electrodes. As expected, when SLBs were formed on the electrodes, the electrical circuital

243   response to alternating voltage shifted from the black (PEDOT:PSS only) to the red (SLB)

244   signal, as shown in Fig. 3a (right). Subsequently, upon the addition of the VPP$_{WH1}$ to the SLB

245   with both ACE2 receptors and TMPRSS2 proteases, the circuital response shifted from red to

246   blue and, when fitted and normalized, the SLB membrane resistance increased from 13.1 to 19.9

247   Ω*cm^2 (+ 51.9 %). We hypothesize that this increase in resistance is attributed to the

248   incorporation of additional biomacromolecules originally in the viral envelope now present in the

249   SLB after the fusion event takes place — an observation that is consistent with optical data under

250   the same conditions (Supplementary Fig. 7). VPP$_{WH1}$ were also added to a SLB containing ACE2

251   (no TMPRSS2 protease) to measure the electrical response arising from binding interactions,

252   while VPP$_{\Delta env}$ were added to the SLB with both ACE2 TMPRSS2 to identify any non-specific

253   interactions between the bilayer and pseudo particles not directed via Spike-ACE2 binding. The

254   electrical responses from both control groups are consistent with optical data as shown in

255   Supplementary Fig. 7, suggesting minimal interactions when compared to fusion. The

256   differences in both electrical and optical signals between binding and fusion events suggest that

257   we can differentiate between them under conditions suitable for the early entry pathway using

258   the electronic label-free approach on our *infection-on-chip* devices.

259   The late entry pathway requires protease CatL, instead of TMPRSS2, to catalyze the

260   virus-membrane fusion. We were able to reproduce this pathway using our model system by

261   supplementing the bulk solution with CatL, which is a soluble protein, and mimicking the acidic

262   endosomal environment in which CatL is active. To mimic this environment and triggering

263   conditions in our platform, we generated SLBs made from Vero E6-derived blebs, which

264   contained the ACE2 receptor but no TMPRSS2. To recreate the endosomal triggering

265   environment, as shown in Fig. 3b, we exchanged the initial pH 7.4 buffer to a more acidic buffer

266   (pH 5.5) and then added soluble CatL, which is active at pH 5.5 but not at pH 7.4. Similar to the

267   early entry pathway, the electrode baselines were acquired before SLB formation (black) and

268   after SLB formation (red), as shown in Fig. 3b (right). VPP$_{WH1}$ were first added to bind with the

269   ACE2 receptors in the SLB at pH 7.4, before exchanging the buffer to a more acidic environment

270   (pH 5.5). As a result, the electrical signal shifted from red to pink, indicating that the binding

271   between ACE2 receptors and the VPP, together with the pH drop contributed to an increase in

272   membrane resistance, aligned with our observation in the early entry pathway (Supplementary

273   Fig. 7) and previous report[33]. Upon the addition of CatL, the SLB membrane resistance further

274   increased (blue trace, from 23.3 to 36.7 Ω*cm^2, + 57.5 %), suggesting successful fusion between

275 the VPPs and SLB membranes. As a control for fusion at non-optimal triggering conditions,

276 CatL was also added to a non-acidic buffer environment after the VPP_{WH1} addition. The

277 electrical signal (Supplementary Fig. 8) suggested membrane resistance dropped insignificantly,

278 indicating there was no fusion due to non-optimal triggering conditions; $VPP_{\Delta env}$ were used as a

279 negative control and no significant membrane resistance shift was observed at lower pH after the

280 addition of CatL (Supplementary Fig. 8). These measurements are all congruent with the optical

281 data (Supplementary Fig. 8). From the electrical and optical data it is clear that both CatL and

282 acidic conditions are required for promoting fusion of the VPP_{WH1} with the SLB, an observation

283 that is consistent with our current understanding of SARS-CoV-2 viral entry[37,38].

284   The repeatability over biological and technical replicates of electrical responses for

285 fusion and control groups for both pathways is shown in Fig 3c. The change in resistance values

286 for fusion events of VPP_{WH1} are comparable in the early (+ 54.0 ±20.0 %) and late entry (+ 42.9

287 ±20.2 %) pathways, both distinct from all control groups.

288

289 **Differentiating between Wuhan-Hu-1, Omicron BA.1, and BA.4 strains using *Infection-on-***

290 ***Chip***

291 The VPP_{WH1} were used in all the entry experiments so far and we have confirmed both entry

292 pathways can be recapitulated using the *Infection-on-Chip* platform. Next, we investigated if our

293 platform was capable of distinguishing SARS-CoV-2 variants with different fusogenicities.

294 Omicron BA.1 and BA.4 (BA.1 and BA.4) were selected in this study since BA.1 has been

295 reported to be less fusogenic than BA.4, while both Omicron variants selected have lower

296 fusogenicities than the WH1[39-41].

297   The electrical readouts modeling the early and late entries of BA.1 are shown in Fig. 4a.

298   Interestingly, we see no significant membrane resistance increase in the case of early pathway

299   (left), yet a small, but distinguishable resistance increase can be observed in the case of late

300   pathway (middle). Statistical data (right) suggested significance between early and late entries of

301   BA.1, matching more recent reports[40,42-45].

302   The resistance values of both early (left) and late (right) entries of BA.4 are shown in Fig.

303   4b. Comparing BA.1 to BA.4 VPP, membrane resistance increases were more significant for

304   VPP$_{BA.4}$, as suggested by statistical data (right), supporting the reports of BA.4 being more

305   fusogenic than BA.1[39,46]. However, when comparing wild type SARS-CoV-2 to the BA.4 strain,

306   shown in Fig 3c, the membrane resistance increase caused by the fusion of VPP$_{BA.4}$ was still

307   significantly reduced: from + 54.0±20.0 % to + 21.4±10.3 % for the early entry pathway and

308   from + 42.9±20.2 % to + 24.6±12.1 % for the late pathway. Our results matched strongly with

309   viral transduction assays as shown in Fig. 4c, where the relative luciferase units detected using

310   the VPP$_{WH1}$ were about 7x higher than VPP$_{BA.1}$ and 4x higher than VPP$_{BA.4}$. A detailed

311   description of the transduction assay is provided in the **Methods** section. Our EIS based fusion

312   assay aligns well with other standard assays used to determine relative infectivity of virus

313   particles, such as syncytia and plaque assays, evaluating the relative fusogenicities of the three

314   variants explored here[39-41], confirming the accuracy of *Infection-on-Chip* platform in

315   distinguishing SARS-CoV-2 variants.

316

317   **Reversing SARS-CoV-2 Early and Late Pathway Configurations**

318   The previous arrangements used the SLB as a model for either the cellular or endosomal

319   membrane surfaces and the VPP as mimics of the infectious virus. Here, we swap the active

320 constituents of both entry pathways, where now the SLB displayed features found on the virus

321 surface (*i.e.,* the glycoproteins), while blebs in the bulk phase presented their respective host cell

322 surfaces. Specifically, we constructed SLBs that contained Spike$_{WH1}$ protein and formed cell

323 blebs that contained ACE2 or ACE2/TMPRSS2 as host cell "particles" that can bind to and fuse

324 with the Spike-containing SLBs. By swapping the constituent presentation, we present an

325 intriguing strategy for rapidly screening cell types and their respective susceptibility to viral

326 infection without the need for virus particles (virus-free) and only the spike protein gene for

327 cellular expression.

328   Spike proteins were incorporated into the SLB by rupturing Spike-transfected HEK293

329 blebs, while TMPRSS2-modified Vero E6 cell blebs (Fig. 5a) and Vero E6 cell blebs (Fig. 5b)

330 were introduced to evaluate and quantify their interactions with the "virus-like" SLB. Mirroring

331 our previous experiments, the SLBs were formed on both PEDOT:PSS coated glass coverslips

332 (Supplementary Fig. 9) and PEDOT:PSS electrodes for optical and electrical readout,

333 respectively.

334   We first investigated the electrical responses for reversed "early entry". Similar to the

335 more traditional display of constituents described earlier, the electrical signal shifted from the

336 electrode baseline (black) to the SLB signal (red) (Fig. 5a). After the addition of cell blebs with

337 ACE2 receptors and TMPRSS2, Spike SLB membrane resistance increased from 20.3 to 31.0

338 Ω*cm^2 (+ 52.7 %), showing a similar membrane resistance increase as measured in early entry

339 pathway as shown in Fig. 3a and 3c. Similarly, in the reversed "late entry", cell blebs with ACE2

340 were added to bind with the Spike SLB and soluble CatL was added to initiate the fusion, after

341 swapping to an acidic buffer environment. The electrical response at each step was measured and

342 plotted in Fig. 5b. After the formation of Spike SLB (red), membrane resistance increased to 51.7

343     $\Omega*\text{cm}^2$ (pink) upon binding with ACE2-containing blebs and exchanging to a lower pH buffer

344   environment (from PBS pH 7.4 to PBS pH 5.5). Membrane resistance increased to 72.1 $\Omega*\text{cm}^2$

345   (blue) after the addition of CatL (+ 39.5 %), comparable to the electrical response of the late

346   entry pathway shown in Fig. 3b and 3c. This work shows the SLB based *infection-on-chip*

347   platform can be used to quickly screen interactions between Spike proteins and host cell

348   membranes without producing VPP or virus-like particles (VLP). This can be especially useful

349   for screening antibodies against Spike protein and small molecule fusion inhibitors in a high

350   throughput manner.

351

Discussion

Infection-on-chip Model

354   The *Infection-on-Chip* devices rely on surface electrodynamics measurements to denote specific

355   interactions between the VPP and the host. To achieve this, the devices were constructed from

356   the necessary biological and chemical elements described earlier and responses were modeled

357   using electrical components of resistors and capacitors. The most rudimentary system resulted in

358   signal contributions from the electrolyte solution resistance and PEDOT:PSS capacitance

359   (electrode baselines in Fig. 2-5). The resistance fluctuations are used as a diagnostic tool to

360   distinguish between the binding and fusion events, the data for which are presented in Fig. 3-5.

361   Although we have not yet identified the mechanism by which binding and fusion lead to

362   an increase in resistance, we hypothesize that it could be via two potential mechanisms: 1) as

363   more material is integrated into the SLB, the increase in protein and lipid density results in an

364   increase in resistance due to tighter packing, or 2) as more proteinaceous and lipid materials are

365   added to the SLB, membrane defects, or "gaps", are filled in, consequently increasing the

366   resistance. Both hypotheses are evinced in the fusion pathways for fusogenic WuHan-Hu-1,

367   where resistance values increased by 40-60%. Conversely, the less significant resistance

368   increases upon binding, shown in Fig. 3c and Supplementary Fig. 7, support the second

369   hypothesis. In this scenario, the ACE2 and VPP interactions result in VPP immobilization

370   proximal to the SLB surface, potentially blocking defects near the binding site, without

371   integrating into the SLB itself, though these experiments are still ongoing. Overall, identifying

372   and characterizing fusion events can be especially beneficial for isolating particularly infectious

373   viral variants or screening for therapeutics that target either event.

374

375   **SARS-CoV Model System**

376   The two known entry pathways of SARS-CoV-2 capture the canonical features of coronavirus'

377   initial infection stages, making it an excellent model system for our study. Though the specific

378   receptors and required triggers vary between viral strains and species, there are fundamental

379   aspects that are conserved. For example, there are currently seven identified human

380   coronaviruses (hCoV), among which the most notable are SARS-CoV and MERS-CoV. Though

381   SARS-CoV and SARS-CoV-2 entry mechanisms share more similarities, both requiring an

382   ACE2 protein for binding, all three coronavirus (SARS-CoV-2, SARS-CoV, and MERS-CoV)

383   share similar fusion mechanisms via TMPRSS2 or CatL activation. Going beyond the

384   Coronaviridae family, viruses from the Orthomyxoviridae and Rhabdoviridae families, such as

385   influenza and VSV respectively, also share similarities with the late entry pathways of SARS-

386   CoV-2, requiring an acidification step to prompt fusion. The *Infection-on-Chip* platform may be

387   leveraged to easily identify cell-types particularly susceptible to each virus, provide mechanistic

388   information into the events that initiate infection, and evaluate differences between emerging

389   variants.

390   The SARS-CoV-2 model system provided an opportunity to determine whether or not the

391   platform can detect variability between different Spike protein variants. Since Omicron variants

392   are now dominant globally, we produced Omicron Spike–incorporating VPP, compared to the

393   Spike$_{Wuhan-Hu-1}$ proteins used for the initial experiments. Experiments were first conducted on

394   Omicron BA.1 variants, which showed a decrease in fusion activity, as evinced by a decreased

395   change in resistance for both early- and late- entry pathways (Fig. 4a), albeit a less significant

396   decrease was observed for the late-entry pathway. Interestingly, this was consistent with recently

397   published findings in which it was identified that Omicron BA.1 and BA.2 variants exhibit an

398   altered entry preference compared to ancestral SARS-CoV-2: preferring endosomal (late) entry

399   pathway as these Omicron variants are less dependent on the TMPRSS2 protease[40,42-45]. Since

400   there are several Omicron variants that have emerged, each with unique sets of mutations, we

401   also evaluated a more fusogenic variant — Omicron BA.4. Strikingly, our data correlated well

402   with these reports, as the change in resistance increased for both pathways when using VPP

403   incorporating Spike$_{Omicron BA.4}$ (Fig. 4b). Our data was not only analogous to existing reports of

404   entry-pathway preference, we were also able to detect fusion variability between WH1, Omicron

405   BA.1, and Omicron BA.4 variants that directly mirrored those reported[39]. In these reports the

406   WH1 exhibited the highest fusogencity, followed by Omicron BA.4, and Omicron BA.1 as the

407   least fusogenic of these mutants. These distinctions further highlight the benefits of using this

408   platform with electrical sensing for straightforward screening of viral mutants, and use the

409   acquired data to distinguish highly infectious mutants from those that are less infectious.

410

Prospects

"Bioprocesses"-on-chip devices, such as cell-on-a-chip, organ-on-a-chip, and tissue-on-a-chip for instance, represent emergent platforms of interest amongst the biomedical and biomaterials community. Among a myriad of other benefits, their recent successes as *in vitro* micro-scale physiological models can potentially transform fields that focus on therapeutic development and personalized medicine. Our proposed infection-on-chip platform complements these existing technologies by providing mechanistic information at the membrane level without relying on downstream effects or signals. In other words, our readouts directly correlate to events at the membrane-virus interface with exquisite control over the participating components (*i.e.,* receptors, environmental conditions, and presented pathogens), how they are presented, and functionality of the participating constituents (i.e. either binding or fusion events between the SLB and VPP). Whether using the more traditional display, in which the SLB is mimicking the cellular surface, or a presentation where the SLB is emulating the viral surface, the *infection-on-chip* platform can be employed as a quantitative scaffold to interrogate biological pathways or as a tool to rapidly screen interactions with a viral or cellular surfaces, both of which should assist determining societal responses as VOC continue to emerge.

Methods

Materials

The 1-palmitoyl-2-oleoyl-sn-glycero-3-phosphocholine (POPC), used for the preparation of fusogenic liposomes, was purchased from Avanti Polar Lipids (700 Industrial Park Dr, Alabaster, AL 35007). Biotechnology grade chloroform was used during the preparation of the POPC liposomes and was purchased from VWR (1050 Satellite Blvd. Suwanee, GA 30024).

434   Whatman Nucleopore polycarbonate filters (50 nm) (Cytiva- Marlborough, MA) were used for

435   liposome extrusion. The octadecyl rhodamine B chloride (R18), used as a lipophilic dye for

436   collecting optical data, was made by Invitrogen purchased from Thermo Fisher Scientific-

437   Waltham, MA . Dulbecco's Modified Eagle Medium (DMEM) was used as a basal medium for

438   cell growth and to produce pseudoparticles, along with Gibco Fetal Bovine Serum (FBS) and

439   Gibco Penicillin-Streptomycin (10,000 U/mL) when indicated. TurboFect, Lipofectamine 2000,

440   and Gibco Opti-MEM were purchased through Life Technologies Thermo Fisher and were used

441   for the necessary transfection protocols described later in this section. Corning Trypsin $1\times$,

442   0.25% Trypsin purchased through VWR, 0.53 mM EDTA in HBSS [-] calcium, magnesium was

443   used as the enzymatic agent during passaging. 4-(2-Hydroxyethyl)piperazine-1-ethanesulfonic

444   acid (HEPES), dithiothreitol (DTT), and formaldehyde solution, used for the preparation of the

445   blebs, were all purchased from MilliporeSigma. VWR 25 mm $\times$ 25 mm glass coverslips were

446   used for the preparation of the supported lipid bilayers and as solid supports for the collection of

447   optical data. The Piranha wash consisted of sulfuric acid (95- 98%, VWR) and hydrogen

448   peroxide (50 wt. % solution, Krackler Scientific). PEDOT:PSS (PH 1000) was purchased from

449   Ossila (Sheffield, UK), (3-Glycidyloxypropyl)trimethoxysilane (GOPS) was purchased from

450   MilliporeSigma.

451   *Buffers and other solutions:*

452   GPMV Buffer A: 2 mM $CaCl_2$, 10 mM HEPES, 150 mM NaCl, pH 7.4

453   GPMV Buffer B: 2 mM $CaCl_2$, 10 mM HEPES, 150 mM NaCl, 25 mM formaldehyde, 2 mM

454   DTT pH 7.4

455   Reaction Buffer A: 137 mM NaCl, 2.7 mM KCl, 10 mM Na_2HPO_4, 1.8 mM KH_2HPO_4, pH 7.4

456   Reaction Buffer B: 137 mM NaCl, 2.7 mM KCl, 10 mM Na_2HPO_4, 1.8 mM KH_2HPO_4, pH 5.8

457   C-DMEM: DMEM, 10 % (v/v) FBS, Penicillin-Streptomycin (200 units/mL and 200 ug/mL)

458   F-DMEM: DMEM, 10 % (v/v) FBS

459   **Cell Culture**

460   African green monkey kidney cells (Vero E6) from ATCC, TMPRSS2 enhanced Vero E6 from

461   the JCRB Cell Bank, and Human embryonic kidney cells (HEK-293T) from ATCC were

462   maintained in C-DMEM at 37 °C in an incubator containing 5% CO_2 and 95% air. All cells were

463   passaged upon reaching 80-95% confluency by first washing the cells with Dulbecco's

464   phosphate-buffered saline (DPBS) and then enzymatically releasing them from the flasks using

465   Trypsin EDTA 1x. Confluency was monitored using bright-field microscopy.

466   **GPMV ('bleb') preparation**

467   GMPVs were prepared using previously established methodologies aimed to produce free

468   GMPVs from attached cells. Once the cells have achieved >90% confluency, in preparation for

469   blebbing, the cells were washed with GMPV buffer A (3x). Freshly prepared GPMV Buffer B

470   was then added to the plate and incubated at 37 °C for 2 hours. Both GPMV Buffer A and

471   GPMV Buffer B contain small amounts of $CaCl_2$, as calcium has been found to be crucial for

472   promoting an optimal fusion environment[47,48]. The buffer, now containing the GPMVs, was

473   decanted into a conical tube and incubated on ice for 45 minutes. Post incubation the top 80% of

474   the solution was collected, and the bottom 20% was disposed. The GMPVs were characterized

475   using dynamic light scattering using a Malvern Panalytical Enigma Business Park, Grovewood

476   Road Malvern, WR14 1XZ, UK Zetasizer MAL1026438 and NanoCyte. New GMPVs were

477   prepared every two weeks to ensure that maximum protein activity was maintained.

478   **Preparation of Pseudotyped Particles**

479 Human embryonic kidney cells HEK293 cells were seeded on 6-well plates with 2 mLs of C-

480 DMEM solution per well. The cell density typically reached ~50% confluence prior to

481 proceeding to the next step. Transfection was performed with three plasmids encoding for the

482 different proteins required to form pseudotyped particles: the envelope glycoprotein, MLV gag

483 and pol proteins, and luciferase reporter. The total amount of DNA per well was 1 ug with 300

484 ng of gagpol, 400 ng of luciferase reporter, and 300 ng of the envelope protein (all sequences

485 encoding for the genes can be found in Supplementary Table 1). First the plasmids encoding for

486 gagpol and luciferace were combined and incubated at room temperature for five minutes. For a

487 50 mL solution, 1.25 mLs of optimem and 1.4 mLs of polyethyleneimine (PEI) were added to a

488 50 mL falcon tube. The envelope proteins were added to the tube as well, appropriately scaling

489 the amount to the 50 mL total volume. The envelope proteins were either SARS-CoV2 spike

490 protein, vesicular stomatitis virus (VSV) G glycoprotein, or a negative control that lacked any

491 enveloped glycoproteins (Δenv). The backbone proteins (gagpol) were then added to the same

492 tube and incubated at room temperature for 20 minutes. F-DMEM was added to a final volume

493 of 50 mLs after the incubation. The C-DMEM was aspirated from the HEK293 cells and washed

494 with F-DMEM prior to adding the transfection mixture. The F-DMEM mixture was then added,

495 where each well on the plate contained a final volume of 2 mLs, and incubated for 48 hours at 37

496 °C. By the end of the incubation period, the cells typically changed color to orange, being careful

497 not to over-incubate (resulting in yellow color). The supernatant was collected from the wells

498 and placed into 50 mL falcon tubes. These tubes were centrifuged for 7 minutes at 290 xg at 4

499 °C. Being careful not to disturb the bottom of the tubes, the supernatant was, once again,

500 recovered and filtered through a 0.22 μm syringe filter. To ensure longevity of the samples, 1 mL

501 aliquots were frozen and stored at -80 °C until needed for use.

Pseudotyped Particle transduction (infectivity) assay

Spike-containing viral pseudoparticles (VPPs$_{spike}$) were produced as mimics of SARS-CoV-2

infectious virions using previously established methodologies[22]. The backbone of the VPPs

consisted of a Murine Leukemia Virus (MLV)-gagpol and the viral envelope contained wtSARS-

CoV2 Spike protein (WH1 strain), referred to as wt in the bar graph here. The interior cavity of

the particles contained a luciferase reporter gene, which allowed for a straightforward method to

test the transduction of the VPPs$_{spike}$. In this assay, once the reporter gene was successfully

delivered and integrated into the host cell's genome, the transduced cells were quantified using a

luciferase activity assay. To perform this assay, African green monkey kidney epithelial Vero-E6

cells were seeded in 24-well plates and incubated until 80-90% confluency was obtained. Each

well was washed with 0.5 mLs of Dulbecco's Phosphate Buffered Saline (DPBS) 3x, inoculated

with 0.2 mLs of undiluted pseudovirus particle solution, and incubated at 37 °C for 1.5 hours

while agitating on a rocker. After the first incubation period was complete, 0.2 mLs of C-DMEM

were added and incubated at 37 °C for 72 hours. The infectivity was assessed using previously

reported luciferase assay. Briefly, the luciferase substrate and 5× Promega lysis buffer were

thawed. The buffer was diluted with sterile water and added to the cells for lysis. For a most

effective lysis, the cells went through several freeze thaw cycles, being transferred from -80 °C

to room temperature 3×. After the last thaw cycle, 10 μL of lysate and 20 μL of Luciferin were

combined in an eppendorf tube and analyzed using a Promega (Durham, NC) GlowMax 20/20

luminometer.

Transfection of plasmids containing SARS-CoV2 Spike

Typically the SARS-CoV2 Spike was transfected into HEK293 cells. For a 10 cm petri dish 400

μL of Opti-MEM was combined with either 24 μL of Lipofectamine and incubated for five

525 minutes at room temperature. In another tube, 8 μg of plasmid was added to 400 μL of Opti-

526 MEM. The two tubes were combined and incubated further for 20 minutes at room temperature.

527 Once the appropriate cells reached ~70% confluency, they were washed with DPBS and the

528 Opti-MEM solution, containing transfection reagent and the plasmid, was added directly to the

529 cells. The cells were incubated at 37 °C for one hour, then 8 mLs of C-DMEM were added to the

530 top of the cells as well. They continued to incubate at 37 °C for 12-16 hours before the next step.

531 **SLB formation on PEDOT:PSS surface**

532 To form SLB with cell blebs on PEDOT:PSS surface, a simultaneous incubation of both blebs

533 and fusogenic vesicles is applied to generate repeatable results. PEDOT:PSS coverslip/ electrode

534 device were soaked in DI for over 24 hours prior to use. Cell blebs and POPC lipids were mixed

535 and sonicated for 20 mins to induce fusion[49,50] before adding onto a light oxygen plasma-treated

536 (Harrick Plasma Inc., Ithaca NY, PDC-32G , 7.2 W, 350 Micron, 1 min) PEDOT:PSS surface. It

537 is worth noting that the plasma condition needs to be tuned for each plasma cleaner, as weak

538 treatment won't provide sufficient hydrophilicity to rupture the blebs and vesicles, while too

539 strong of a treatment will render the surface more negative and rough, making it challenging for

540 the often negative native components to self assemble into a mobile SLB. The incubation time

541 for SLB formation on PEDOT:PSS surface was 1 hour before excess materials were rinsed out

542 with PBS buffer prior to further characterizations. The presence of native membrane components

543 in SLB was verified using TIRF as shown in Fig. 2b.

544 **FRAP analysis**

545 Prior to SLB formation described in the previous method, the blebs were sonicated for 30

546 minutes (kept under 25 ˚C with ice pad) to incorporate the lipophilic dye octadecyl rhodamine B

547 chloride (R18) into the blebs (1 μL of 0.5 mg/mL R18 into 100 μL of blebs). SLB formation

548   proceeded as previously described. To verify formation of the SLB and confirm lipid mobility,

549   an inverted Zeiss Axio Observer Z1 microscope was used with a 20× objective lens. A 20 μm

550   diameter was bleached for 500 ms and the recovery was monitored for 30 minutes. The

551   fluorescence intensity was recorded and normalized. The data was fit to a standard Bessel

552   function and diffusion (D) was determined using the equation: $D = w^2 / 4t_{1/2}$, where w represents

553   the width (diameter) of the bleach spot, and $t_{1/2}$ is the time it took for the fluorescence to recover

554   to half of the maximum intensity, and D is the determined diffusion measurement.

555   **TIRF microscopy**

556   SLBs were prepared (without the R18 dye as previously described). The pseudoparticles were

557   first labeled by sonicating with R18 dye (1 μL of 0.5 mg/mL for 100 μL of pseudo particle

558   solution) for 30 minutes (kept under 25 ˚C with ice pad). For this assay, the VPPs are labeled to a

559   semi-quenched state (independently verified using a fluorimeter (Supplementary Fig. 10)), where

560   the fluorescence intensity is adequate to observe the particles within the TIRF field of view

561   (FOV) but not proportional to the extent of labeling. The excess dye was removed using a size-

562   exclusion column or simply washed away when appropriate. TIRF measurements were

563   performed on Zeiss Axio Observer.Z1 microscope using an α Plan-Apochromat 100x objective

564   with a numerical aperture (NA) of 1.46. The samples were excited with a 561 nm laser and the

565   angle of incidence was adjusted to ~68° to insure an evanescent wave of 100 nm with total

566   internal reflection. Prior to acquiring these images, we washed our experimental well with

567   excessive buffer to remove any unbound particles and ensure that we were acquiring images of

568   only those particles that were bound and not diffusing in/out of the FOV.

569   **Microelectrode fabrication**

570   Gold contact pads were patterned on fused silica wafer using a standard photolithography

571   procedure: exposure, develop, deposition, and lift-off[51]. A 200 nm of SiO_2 insulating layer was

572   then deposited ubiquitously on Au patterned wafer using plasma enhanced chemical vapor

573   deposition (PECVD). A second layer of photolithography was applied to define the PEDOT:PSS

574   electrode locations on the gold contact pad, followed by the reactive ion etching of SiO_2 until it

575   reached the gold surface. PEDOT:PSS mixed with 1 v/v % of GOPS was then spin-coated at

576   4000 rpm on both exposed gold contact and SiO_2 insulating layer, followed by the annealing at

577   140 ˚C for 30 mins to drive off all water. A third layer of photolithography was applied to

578   remove the PEDOT:PSS spun on SiO_2, taking advantage of the germanium (Ge) hard mask

579   protocol previously reported[52]. The 100 nm thick protective Ge hard mask on PEDOT:PSS

580   electrode was then removed by immersing in deionized water for 48 hours.

581   **EIS Measurement and Data Analysis**

582   An Autolab PGSTAT302N potentiostat was used to conduct the EIS measurements. The

583   frequency of applied sinusoidal voltage was swept from 10^6 Hz to 1 Hz to capture the change in

584   electrical signal at each step after the addition of biological materials. Prior to SLB formation,

585   the PEDOT:PSS electrode baseline was measured and fitted into a RC circuit. Signals after SLB

586   formation were fit to a RC(RC) circuit, where membrane resistance and capacitance were

587   extracted. Vigorous rinsing with PBS buffer was done before each measurement at every step

588   after SLB formation, 20 mins after adding VLPs or cell blebs and 30 mins after adding CatL.

589

590   **Data availability**

591   The data supporting the findings of this study are available within the paper and supplementary

592   information (Fig. 1-12 and Table 1).

593

References

595   1   Domingo, E., García-Crespo, C., Lobo-Vega, R. & Perales, C. Mutation Rates, Mutation
596   Frequencies, and Proofreading-Repair Activities in RNA Virus Genetics. *Viruses* **13**, 1882 (2021).
597   2   Drake, J. W. & Holland, J. J. Mutation rates among RNA viruses. *Proceedings of the National*
598   *Academy of Sciences* **96**, 13910-13913, doi:doi:10.1073/pnas.96.24.13910 (1999).
599   3   Elena, S. F. & Sanjuan, R. Adaptive value of high mutation rates of RNA viruses: separating causes
600   from consequences. *J Virol* **79**, 11555-11558, doi:10.1128/JVI.79.18.11555-11558.2005 (2005).
601   4   Shahabipour, F. *et al.* Engineering organ-on-a-chip systems to model viral infections.
602   *Biofabrication* **15**, doi:10.1088/1758-5090/ac6538 (2023).
603   5   Si, L. *et al.* A human-airway-on-a-chip for the rapid identification of candidate antiviral
604   therapeutics and prophylactics. *Nat Biomed Eng* **5**, 815-829, doi:10.1038/s41551-021-00718-9
605   (2021).
606   6   Tan, J. *et al.* Biomimetic lung-on-a-chip to model virus infection and drug evaluation. *Eur J Pharm*
607   *Sci* **180**, 106329, doi:10.1016/j.ejps.2022.106329 (2023).
608   7   Jackson, C. B., Farzan, M., Chen, B. & Choe, H. Mechanisms of SARS-CoV-2 entry into cells.
609   *Nature Reviews Molecular Cell Biology* **23**, 3-20, doi:10.1038/s41580-021-00418-x (2022).
610   8   Nolan, T., Hands, R. E. & Bustin, S. A. Quantification of mRNA using real-time RT-PCR. *Nature*
611   *protocols* **1**, 1559-1582 (2006).
612   9   Amanat, F. *et al.* A serological assay to detect SARS-CoV-2 seroconversion in humans. *Nature*
613   *medicine* **26**, 1033-1036 (2020).
614   10   Diao, B. *et al.* Accuracy of a nucleocapsid protein antigen rapid test in the diagnosis of SARS-CoV-
615   2 infection. *Clinical Microbiology and Infection* **27**, 289. e281-289. e284 (2021).
616   11   Chen, Y. *et al.* Impact of SARS-CoV-2 variants on the analytical sensitivity of rRT-PCR assays.
617   *Journal of Clinical Microbiology* **60**, e02374-02321 (2022).
618   12   Zou, Y., Mason, M. G. & Botella, J. R. Evaluation and improvement of isothermal amplification
619   methods for point-of-need plant disease diagnostics. *PloS one* **15**, e0235216 (2020).
620   13   Gootenberg, J. S. *et al.* Nucleic acid detection with CRISPR-Cas13a/C2c2. *Science* **356**, 438-442
621   (2017).
622   14   Yousefi, H. *et al.* Detection of SARS-CoV-2 viral particles using direct, reagent-free
623   electrochemical sensing. *Journal of the American Chemical Society* **143**, 1722-1727 (2021).
624   15   Ventura, B. D. *et al.* Colorimetric test for fast detection of SARS-CoV-2 in nasal and throat swabs.
625   *ACS sensors* **5**, 3043-3048 (2020).
626   16   Dziąbowska, K., Czaczyk, E. & Nidzworski, D. Detection methods of human and animal influenza
627   virus—current trends. *Biosensors* **8**, 94 (2018).
628   17   Zhou, F. *et al.* A Supported Lipid Bilayer-Based Lab-on-a-Chip Biosensor for the Rapid Electrical
629   Screening of Coronavirus Drugs. *ACS Sens* **7**, 2084-2092, doi:10.1021/acssensors.2c00970 (2022).
630   18   Wrapp, D. *et al.* Cryo-EM structure of the 2019-nCoV spike in the prefusion conformation.
631   *Science* **367**, 1260-1263, doi:doi:10.1126/science.abb2507 (2020).
632   19   Hoffmann, M. *et al.* SARS-CoV-2 Cell Entry Depends on ACE2 and TMPRSS2 and Is Blocked by a
633   Clinically Proven Protease Inhibitor. *Cell* **181**, 271-280.e278,
634   doi:https://doi.org/10.1016/j.cell.2020.02.052 (2020).
635   20   Shulla, A. *et al.* A Transmembrane Serine Protease Is Linked to the Severe Acute Respiratory
636   Syndrome Coronavirus Receptor and Activates Virus Entry. *Journal of Virology* **85**, 873-882,
637   doi:doi:10.1128/jvi.02062-10 (2011).

638 21 Bayati, A., Kumar, R., Francis, V. & McPherson, P. S. SARS-CoV-2 infects cells after viral entry via
639   clathrin-mediated endocytosis. *Journal of Biological Chemistry* **296**, 100306,
640   doi:https://doi.org/10.1016/j.jbc.2021.100306 (2021).
641 22 Au - Millet, J. K. *et al.* Production of Pseudotyped Particles to Study Highly Pathogenic
642   Coronaviruses in a Biosafety Level 2 Setting. *JoVE*, e59010, doi:doi:10.3791/59010 (2019).
643 23 Zhang, Y. *et al.* Supported Lipid Bilayer Assembly on PEDOT:PSS Films and Transistors. *Advanced*
644   *Functional Materials* **26**, 7304-7313, doi:https://doi.org/10.1002/adfm.201602123 (2016).
645 24 Liu, H.-Y. *et al.* Self-Assembly of Mammalian-Cell Membranes on Bioelectronic Devices with
646   Functional Transmembrane Proteins. *Langmuir* **36**, 7325-7331,
647   doi:10.1021/acs.langmuir.0c00804 (2020).
648 25 Zhao, Z., Spyropoulos, G. D., Cea, C., Gelinas, J. N. & Khodagholy, D. Ionic communication for
649   implantable bioelectronics. *Science Advances* **8**, eabm7851, doi:doi:10.1126/sciadv.abm7851
650   (2022).
651 26 Rochford, A. E. *et al.* Functional neurological restoration of amputated peripheral nerve using
652   biohybrid regenerative bioelectronics. *Science Advances* **9**, eadd8162,
653   doi:doi:10.1126/sciadv.add8162 (2023).
654 27 Costello, D. A., Hsia, C.-Y., Millet, J. K., Porri, T. & Daniel, S. Membrane Fusion-Competent Virus-
655   Like Proteoliposomes and Proteinaceous Supported Bilayers Made Directly from Cell Plasma
656   Membranes. *Langmuir* **29**, 6409-6419, doi:10.1021/la400861u (2013).
657 28 Costello, D. A., Millet, J. K., Hsia, C.-Y., Whittaker, G. R. & Daniel, S. Single particle assay of
658   coronavirus membrane fusion with proteinaceous receptor-embedded supported bilayers.
659   *Biomaterials* **34**, 7895-7904, doi:https://doi.org/10.1016/j.biomaterials.2013.06.034 (2013).
660 29 Ogando, N. S. *et al.* SARS-coronavirus-2 replication in Vero E6 cells: replication kinetics, rapid
661   adaptation and cytopathology. *Journal of General Virology* **101**, 925-940,
662   doi:https://doi.org/10.1099/jgv.0.001453 (2020).
663 30 Matsuyama, S. *et al.* Enhanced isolation of SARS-CoV-2 by TMPRSS2-expressing cells.
664   *Proceedings of the National Academy of Sciences* **117**, 7001-7003,
665   doi:doi:10.1073/pnas.2002589117 (2020).
666 31 Proctor, C. M., Rivnay, J. & Malliaras, G. G. Understanding volumetric capacitance in conducting
667   polymers. *Journal of Polymer Science Part B: Polymer Physics* **54**, 1433-1436,
668   doi:https://doi.org/10.1002/polb.24038 (2016).
669 32 Manzer, Z. A. *et al.* Cell-Free Synthesis Goes Electric: Dual Optical and Electronic Biosensor via
670   Direct Channel Integration into a Supported Membrane Electrode. *ACS Synthetic Biology* **12**, 502-
671   510, doi:10.1021/acssynbio.2c00531 (2023).
672 33 Tang, T. *et al.* Functional Infectious Nanoparticle Detector: Finding Viruses by Detecting Their
673   Host Entry Functions Using Organic Bioelectronic Devices. *ACS Nano* **15**, 18142-18152,
674   doi:10.1021/acsnano.1c06813 (2021).
675 34 Lubrano, C., Matrone, G. M., Iaconis, G. & Santoro, F. New Frontiers for Selective Biosensing with
676   Biomembrane-Based Organic Transistors. *ACS Nano* **14**, 12271-12280,
677   doi:10.1021/acsnano.0c07053 (2020).
678 35 Lindholm-Sethson, B. Electrochemistry at Ultrathin Organic Films at Planar Gold Electrodes.
679   *Langmuir* **12**, 3305-3314, doi:10.1021/la951026k (1996).
680 36 Gritsch, S., Nollert, P., Jähnig, F. & Sackmann, E. Impedance Spectroscopy of Porin and
681   Gramicidin Pores Reconstituted into Supported Lipid Bilayers on Indium–Tin-Oxide Electrodes.
682   *Langmuir* **14**, 3118-3125, doi:10.1021/la9710381 (1998).
683 37 Lowther, J. *et al.* The Importance of pH in Regulating the Function of the Fasciola hepatica
684   Cathepsin L1 Cysteine Protease. *PLOS Neglected Tropical Diseases* **3**, e369,
685   doi:10.1371/journal.pntd.0000369 (2009).

686   38   Simmons, G. *et al.* Inhibitors of cathepsin L prevent severe acute respiratory syndrome
687   coronavirus entry. *Proceedings of the National Academy of Sciences* **102**, 11876-11881,
688   doi:doi:10.1073/pnas.0505577102 (2005).
689   39   Park, S. B. *et al.* SARS-CoV-2 omicron variants harbor spike protein mutations responsible for
690   their attenuated fusogenic phenotype. *Communications Biology* **6**, 556, doi:10.1038/s42003-
691   023-04923-x (2023).
692   40   Suzuki, R. *et al.* Attenuated fusogenicity and pathogenicity of SARS-CoV-2 Omicron variant.
693   *Nature* **603**, 700-705, doi:10.1038/s41586-022-04462-1 (2022).
694   41   Wang, X.-J. *et al.* Neutralization sensitivity, fusogenicity, and infectivity of Omicron subvariants.
695   *Genome Medicine* **14**, 146, doi:10.1186/s13073-022-01151-6 (2022).
696   42   Hu, B. *et al.* Spike mutations contributing to the altered entry preference of SARS-CoV-2 omicron
697   BA.1 and BA.2. *Emerging Microbes & Infections* **11**, 2275-2287,
698   doi:10.1080/22221751.2022.2117098 (2022).
699   43   Meng, B. *et al.* Altered TMPRSS2 usage by SARS-CoV-2 Omicron impacts infectivity and
700   fusogenicity. *Nature* **603**, 706-714, doi:10.1038/s41586-022-04474-x (2022).
701   44   Willett, B. J. *et al.* SARS-CoV-2 Omicron is an immune escape variant with an altered cell entry
702   pathway. *Nature Microbiology* **7**, 1161-1179, doi:10.1038/s41564-022-01143-7 (2022).
703   45   Mizuki, Y. *et al.* SARS-CoV-2 Omicron spike H655Y mutation is responsible for enhancement of
704   the endosomal entry pathway and reduction of cell surface entry pathways. *bioRxiv*,
705   2022.2003.2021.485084, doi:10.1101/2022.03.21.485084 (2022).
706   46   Kimura, I. *et al.* Virological characteristics of the SARS-CoV-2 Omicron BA.2 subvariants, including
707   BA.4 and BA.5. *Cell* **185**, 3992-4007.e3916, doi:https://doi.org/10.1016/j.cell.2022.09.018
708   (2022).
709   47   Straus, M. R. *et al.* Ca^{2+} Ions Promote Fusion of Middle East Respiratory Syndrome
710   Coronavirus with Host Cells and Increase Infectivity. *Journal of Virology* **94**, 10.1128/jvi.00426-
711   00420, doi:doi:10.1128/jvi.00426-20 (2020).
712   48   Lai, A. L., Millet, J. K., Daniel, S., Freed, J. H. & Whittaker, G. R. The SARS-CoV Fusion Peptide
713   Forms an Extended Bipartite Fusion Platform that Perturbs Membrane Order in a Calcium-
714   Dependent Manner. *Journal of Molecular Biology* **429**, 3875-3892,
715   doi:https://doi.org/10.1016/j.jmb.2017.10.017 (2017).
716   49   Pace, H. *et al.* Preserved Transmembrane Protein Mobility in Polymer-Supported Lipid Bilayers
717   Derived from Cell Membranes. *Analytical Chemistry* **87**, 9194-9203,
718   doi:10.1021/acs.analchem.5b01449 (2015).
719   50   Thorsteinsson, K., Olsén, E., Schmidt, E., Pace, H. & Bally, M. FRET-Based Assay for the
720   Quantification of Extracellular Vesicles and Other Vesicles of Complex Composition. *Analytical
721   Chemistry* **92**, 15336-15343, doi:10.1021/acs.analchem.0c02271 (2020).
722   51   Thompson, L. F. in *Introduction to Microlithography* Vol. 219 *ACS Symposium Series* Ch. 1, 1-13
723   (AMERICAN CHEMICAL SOCIETY, 1983).
724   52   Thiburce, Q., Melosh, N. & Salleo, A. Wafer-scale microfabrication of flexible organic
725   electrochemical transistors. *Flexible and Printed Electronics* **7**, 034001, doi:10.1088/2058-
726   8585/ac808a (2022).

727

Acknowledgements

742   **Author information**

743   Authors and Affiliations

744   **Robert Frederick Smith School of Chemical and Biomolecular Engineering, Cornell**

745   **University, 124 Olin Hall, Ithaca, NY 14853, USA**

746   Zhongmou Chao, Ekaterina Selivanovitch, Ambika Pachaury & Susan Daniel

747

748   **Department of Chemical Engineering and Biotechnology, University of Cambridge,**

749   **Philippa Fawcett Dr., Cambridge CB3 0AS, UK**

750   Konstantinos Kallitsis, Zixuan Lu & Róisín Owens

751

Contributions

Conceptualization: Zhongmou Chao, Ekaterina Selivanovitch, Konstantinos Kallitsis, Zixuan Lu, Róisín Owens, Susan Daniel

Methodology: Zhongmou Chao, Ekaterina Selivanovitch

Investigation: Zhongmou Chao, Ekaterina Selivanovitch, Ambika Pachaury

Visualization: Zhongmou Chao, Ekaterina Selivanovitch

Supervision: Róisín Owens, Susan Daniel

Writing—original draft: Zhongmou Chao, Ekaterina Selivanovitch, Susan Daniel

Writing—review & editing: Zhongmou Chao, Ekaterina Selivanovitch, Konstantinos Kallitsis, Zixuan Lu, Ambika Pachaury, Róisín Owens, Susan Daniel

Corresponding author

Correspondence to Susan Daniel.

Competing interests
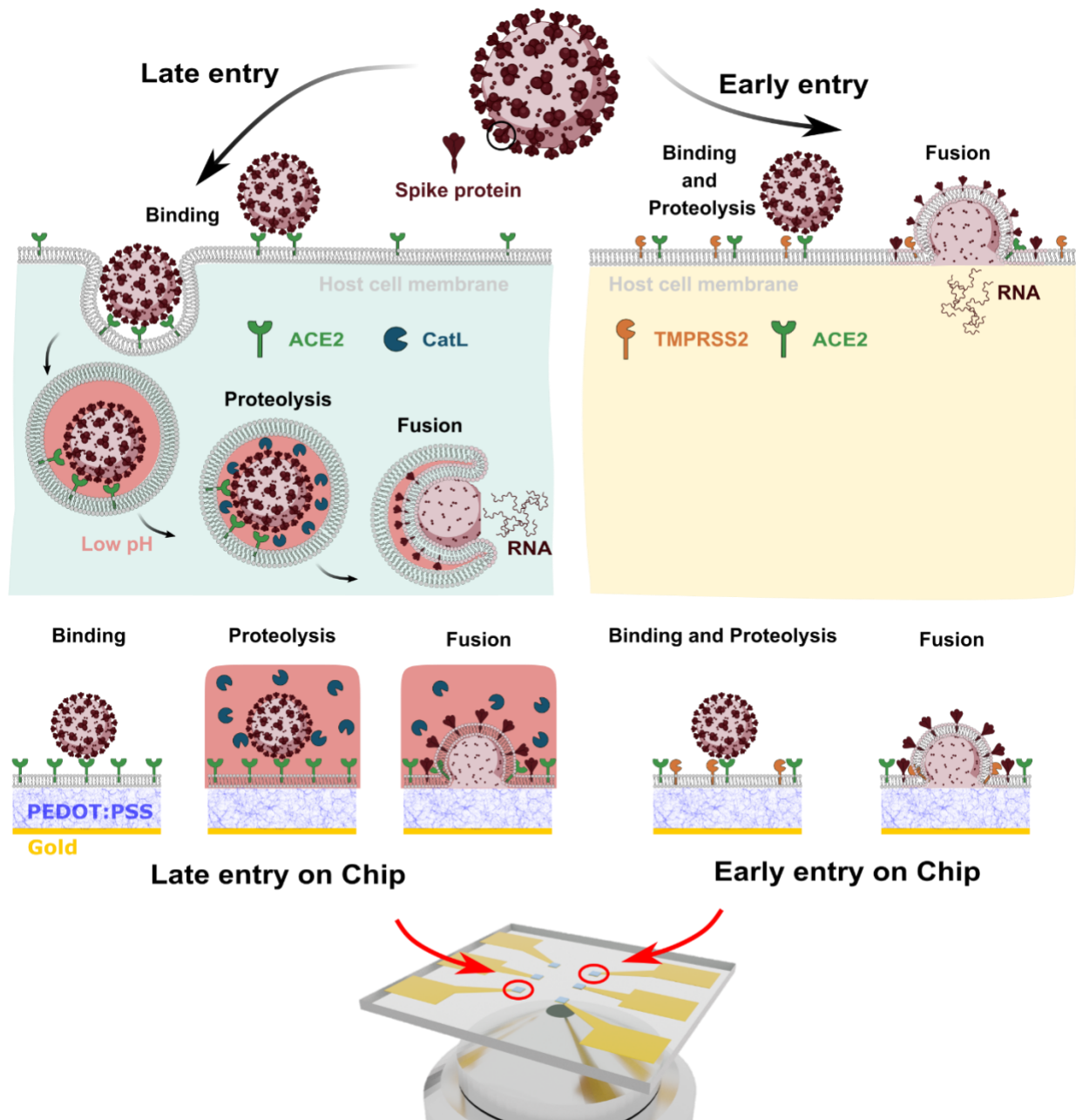
All other authors declare they have no competing interests.

Figures

Fig. 1. SARS-CoV2 entry pathways and the components needed to recapitulate these entry routes in an *in-vitro* platform. The two known pathways of SARS-CoV-2 including early entry, in which fusion is triggered by the TMPRSS2 protease, and late entry, in which virus particle fusion is catalyzed by the protease CatL at low pH (note: pink color = acidic environment). We propose SLBs self-assembled on PEDOT:PSS electrode provide an ideal *infection-on-chip*

776   platform. The SLB is formed using cell-derived blebs and fusogenic vesicles on PEDOT:PSS

777   surface, hence the membrane components are preserved. Viral pseudoparticles (VPP) with Spike

778   protein, pH swap and soluble catalyst (CatL) can be included to induce fusion. The optically

779   transparent and conductive nature of PEDOT:PSS also allowed both optical and electrical

780   readouts to identify trends characteristic of binding and fusion events.

781

782

783
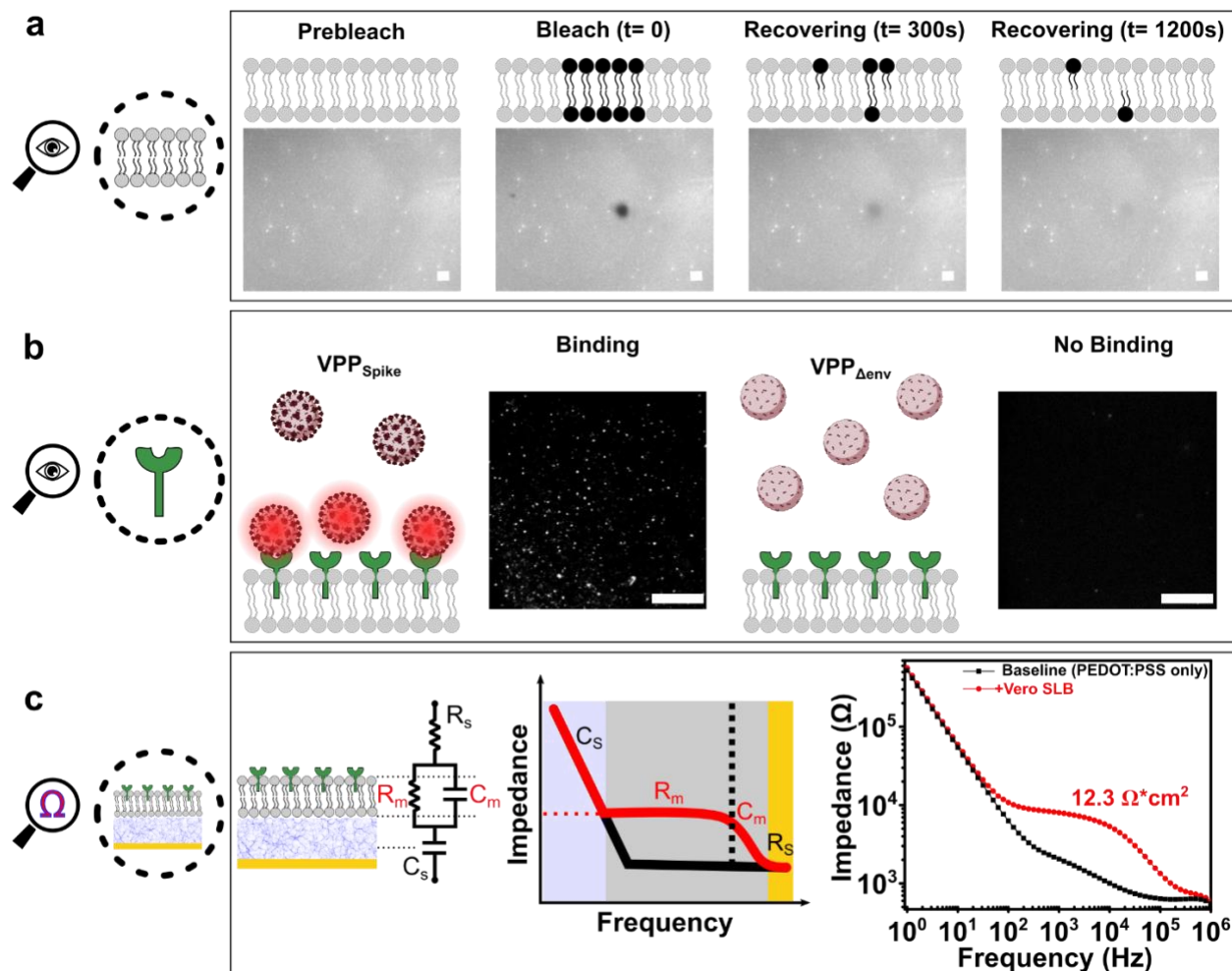
784

785   **Fig. 2. Optical and electrical characterization of the *infection-on-chip* platform's**

786   **components and functionalities.** (**a**) We used FRAP to characterize the mobility of SLBs

787   formed on PEDOT:PSS surfaces. Shown here is a photobleached spot recovering over time,

788   indicating a mobile SLB. The cartoon representation is meant to provide a conceptual illustration

789   of the technique. Indeed, our SLB was composed of both fluorescent and non-fluorescent lipids

790   and the fluorescence seen in the images are reflective of only the doped in R18 dye. (**b**) TIRF

791   was used to confirm the existence of ACE2 receptor in SLBs: only fluorescently labeled VPP_{Spike}

792   are visible at the SLB interface when bound to ACE2 receptors, while no fluorescently labeled

793    $VPP_{\Delta env}$ were observed near the SLB due to the lack of binding interaction with ACE2 receptors

794   on SLB. (**c**) EIS was used to characterize the electrical properties of an SLB on a PEDOT:PSS

795   electrode. An SLB is modeled electrically as a capacitor and a resistor connectedly in parallel,

796   hence its resistance (R_m) can be extracted by fitting into the RC(RC) circuit as shown, it can then

797   be normalized by the area of electrode. All scale bars in this figure represent 20 μm.

798

799

Fig. 3. Electrical responses of fusion via early and late entry pathways recapitulated on host cell derived SLB. (**a**) The experimental group for early fusion pathway consisted of VPP$_{Spike}$ and an SLB containing ACE2 (green) and TMPRSS2 (yellow). EIS Signals are characteristic of

804   fusion events showing the changes in SLB membrane resistance in the equivalent electrical

805   circuit scenario; (**b**) the experimental group consisted of the VPP$_{Spike}$ and an SLB containing

806   ACE2 (green) and CatL (navy), where signals are characteristic impedance data of fusion events

807   (note: pink color = acidic environment); **(c)** distribution of membrane resistance changes at all

808   events of all systems (3 biological replicates and n $\geq$ 8 for all systems) using Spike protein from

809   SARS-CoV-2 Wuhan-Hu-1. ΔR data are mean $\pm$ SD; statistical analysis was performed using

810   one-way analysis of variance (ANOVA) with Šidák's multiple comparisons test, **** (p <

811   0.0001), ns = non-significant.

812

813
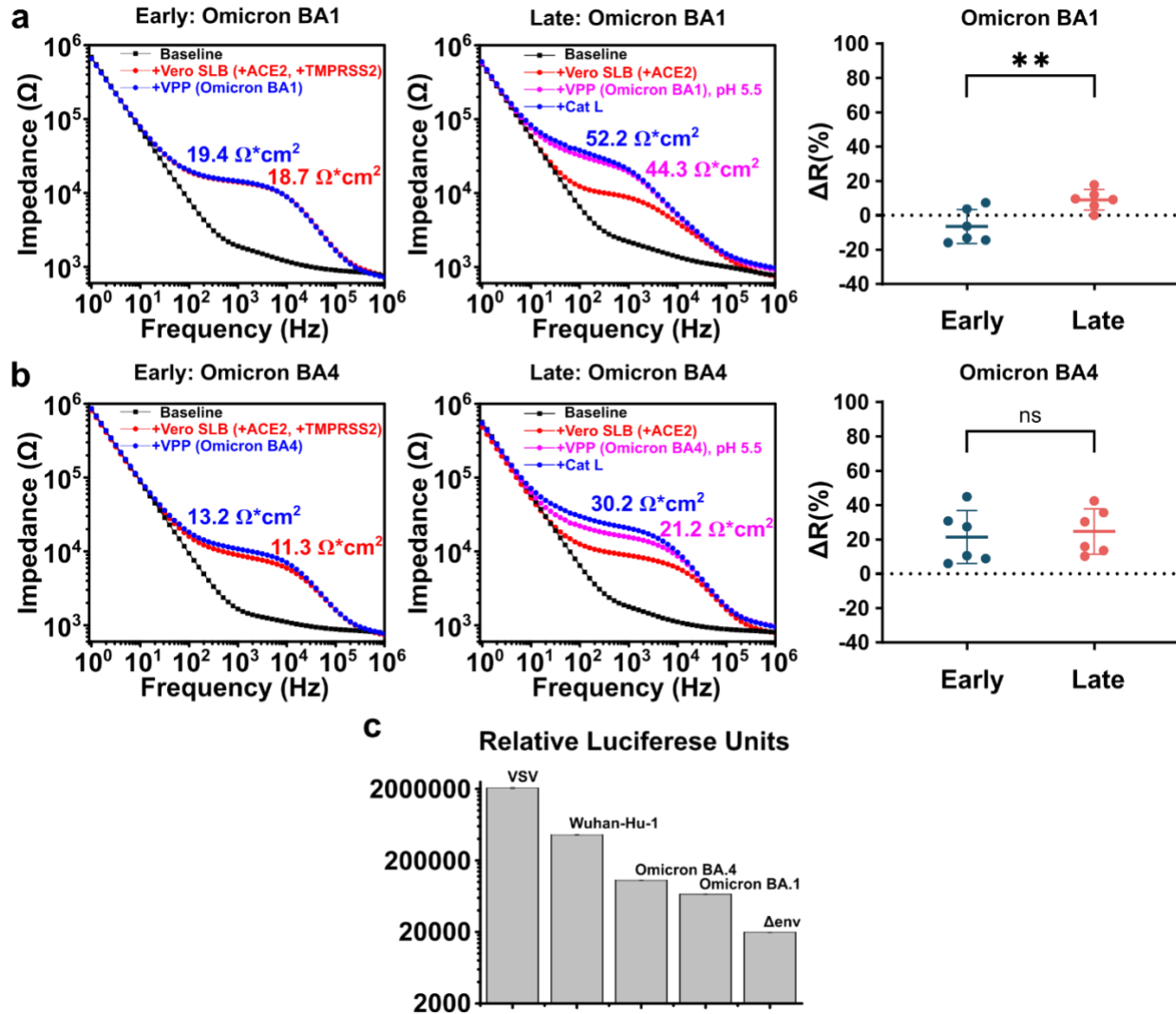
Fig. 4. A comparison of viral fusogenicities of SARS-CoV-2 VOC by electrical response and viral transduction assays. **(a)** EIS electrical signal change of fusion via early (left), late (middle) entry pathways and their statistical comparison (right, n = 6 for both pathways) using Omicron BA.1 VPP; **(b)** EIS electrical signal change of fusion via early (left), late (middle) entry pathways and their statistical comparison (right, n = 6 for both pathways) using Omicron BA.4 VPP. ΔR data are mean ± SD; statistical analysis was performed using one-way analysis of variance (ANOVA) with Šidák's multiple comparisons test, ** (p < 0.01), ns = non-significant; **(c)** relative transduction efficiencies of the Wuhan-Hu-1 Spike and Omicron variant Spike-

823 containing pseudoparticles. The transduction efficiency of VPP$_{Spike}$ was assessed against a

824 positive control that contained a vesicular stomatitis virus G protein (VPP$_{VSV}$) and a negative

825 control without any envelope protein (VPP$_{\Delta env}$). The luciferase production of the infectious

826 VPP$_{Spike}$ and VPP$_{VSV}$ was consistently orders of magnitude higher than VPP$_{\Delta env}$, indicating that

827 the particles we produced were "active" and capable of fusion with a cell membrane. The

828 samples labeled BA.1 and BA.4 refer to Omicron variants. All infectivity assays were completed

829 with Vero E6 TMPRSS2 cell lines. All data above represent five technical replicates (n = 5).

830 Error bars represent standard deviation.

831

832
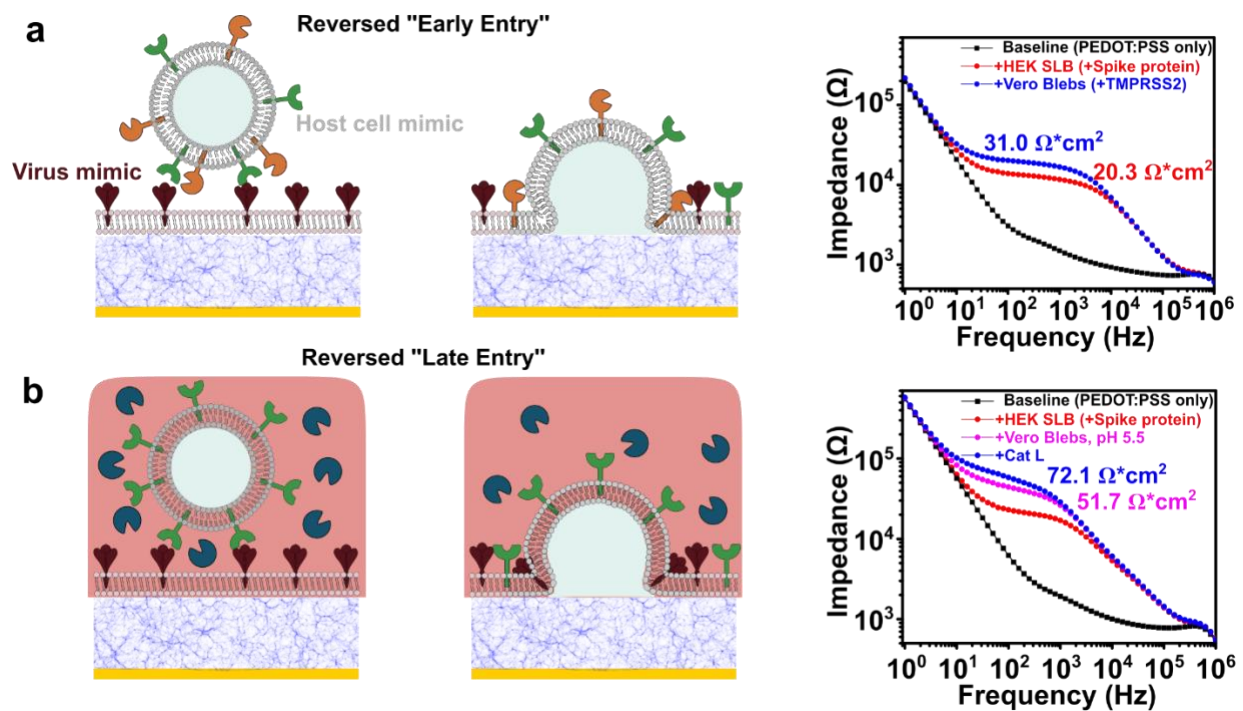
833

834 **Fig. 5**. **Reverse geometry fusion studies using SLB containing Spike protein with different**

835 **blebs**. (**a**) Illustration of "reversed" early entry pathway and its corresponding EIS electrical

836 signal change; (**b**) "reversed" late pathway and the corresponding EIS electrical signal change.